

1 An optimal volumetric constraint ratio with
2 implementation using mixed FE-Meshfree formulation

3 Wu Junchao^{a,*}, Chu Yingjie¹, Xu Yangtao^a, Wang Dongdong¹

^a Key Laboratory for Intelligent Infrastructure and Monitoring of Fujian Province, College
of Civil Engineering, Huaqiao University , Xiamen, Fujian, 361021, China

4 **Abstract**

5 Formulations for incompressible materials often suffer from volumetric locking,
6 leading to reduced accuracy and oscillatory displacement and pressure solutions.
7 A well-chosen constraint ratio can mitigate this issue, but traditional approaches
8 lack a theoretical foundation based on the inf-sup (or LBB) condition, which is
9 essential for the stability of mixed formulations. This paper introduces a novel
10 optimal constraint ratio derived from the inf-sup condition to address volumet-
11 ric locking. The inf-sup test, a numerical tool for verifying the inf-sup condition,
12 is reaffirmed as equivalent to inf-sup condition through a variational approach.
13 By incorporating a complete polynomial space whose dimension matches the
14 number of displacement degrees of freedom (DOFs), a new inf-sup value estima-
15 tor is developed, explicitly considering the constraint ratio. For a given number
16 of displacement DOFs, ensuring that the pressure DOFs remain below a sta-
17 bilized number falls within the optimal constraint ratio range can satisfy the
18 inf-sup condition. To implement of optimal constraint ratio, a mixed finite ele-
19 ment and meshfree formulation is proposed, where displacements are discretized
20 using traditional finite element approximations, and pressures are approximated
21 via the reproducing kernel meshfree method. Leveraging the globally smooth
22 reproducing kernel shape functions, the constraint ratio can be flexibly adjusted
23 to meet the inf-sup condition without the limit of element. For computational
24 efficiency and ease of implementation, pressure nodes are placed on selected
25 displacement nodes to maintain the optimal constraint ratio. Inf-sup tests and
26 a series of 2D and 3D elasticity examples validate the proposed constraint ratio,
27 demonstrating its effectiveness in eliminating volumetric locking and enhancing
28 the performance of mixed finite element and meshfree formulations.

29 *Keywords:* Optimal constraint ratio, Inf-sup condition estimator, Volumetric
30 locking, Mixd formulation, Reproducing kernel meshfree approximation

*Corresponding author
Email address: jcwu@hqu.edu.cn (Wu Junchao)

31 **1. Introduction**

32 The volumetric constraint is a necessary condition in the formulation of
 33 incompressible materials like rubber and hydrogel. Proper imposition of this
 34 constraint is crucial for obtaining better numerical solutions; insufficient or ex-
 35 cessive constraints will reduce the accuracy and stability of the solution [1]. The
 36 volumetric constraint ratio [2], denoted as r , is often used to measure the level
 37 of constraint. It is defined as the total degrees of freedom (DOFs) of displace-
 38 ment divided by the total DOFs of pressure. Ideally, the optimal constraint
 39 ratio should be consistent with its governing partial differential equations. For
 40 example, in the two-dimensional (2D) case, the optimal constraint ratio is 2,
 41 since there are two governing equations for displacement and one for pressure.
 42 When the constraint ratio is less than 2, the formulation suffers from volumetric
 43 locking, while a constraint ratio greater than 2 can cause a coarse solution for
 44 pressure. These observations have been summarized by pioneering work [2] as
 45 follows:

$$r = \frac{2n_u}{n_p}, \quad \begin{cases} r > 2 & \text{too few constraints} \\ r = 2 & \text{optimal} \\ r < 2 & \text{too many constraints} \\ r \leq 1 & \text{severe locking} \end{cases} \quad (1)$$

46 where n_u and n_p are the number of control nodes for displacement and pressure,
 47 respectively. Classifying the locked status via the constraint ratio is straight-
 48 forward but imprecise. For instance, the constraint ratio can remain 2 while
 49 the pressure is discretized using continuous shape functions identical to the
 50 displacement's approximation. However, volumetric locking still exists in this
 51 formulation [2].

52 The inf-sup condition, also known as the Ladyzhenskay–Babuška–Brezzi
 53 (LBB) condition [3, 4], is a more precise requirement for a locking-free for-
 54 mulation. This condition is based on the mixed formulation framework, and
 55 when the inf-sup condition is satisfied, both the accuracy and stability of the
 56 mixed-formulation can be ensured. However, verifying the inf-sup condition is
 57 non-trivial. An eigenvalue problem namely inf-sup test can be used to check
 58 this condition numerically [5, 6, 7, 8]. Analytically, Brezzi and Fortin proposed
 59 a two-level projection framework that always satisfies the inf-sup condition, al-
 60 lowing it to be checked by identifying whether the formulation is included in
 61 this framework. Both analytical and numerical methods to check the inf-sup
 62 condition are complex, and the relationship between the constraint ratio and
 63 the inf-sup condition remains unclear.

64 To address volumetric constraint issues, adjusting the constraint ratio to an
 65 appropriate level is commonly used and easily implemented. In traditional finite
 66 element methods (FEM), this adjustment is carried out based on elements since
 67 the DOFs are embedded in each element. Conventional FEM often exhibits
 68 an over-constrained status. Reducing the approximation order of pressure in
 69 mixed formulation can alleviate the constraint burden, such as with the well-
 70 known Q4P1 (4-node quadrilateral displacement element with 1-node piecewise

constant pressure element) and Q8P3. Globally, using continuous shape functions to link the local pressure DOFs in each element can also reduce the total number of pressure DOFs and increase the constraint ratio, such as with T6P3 (6-node triangular displacement element with 3-node continuous linear pressure element) and Q9P4 (Taylor–Hood element) [9]. These schemes belong to the mixed formulation framework and can also be implemented through a projection approach, where the pressure approximant is projected into a lower-dimensional space. Examples include selective integration methods [10, 11], B–bar or F–bar methods [12, 13, 14, 15, 16], pressure projection methods [17, 18], and the enhanced strain method [19]. Meanwhile, conventional 3-node triangular elements arranged in a regular cross pattern can also reduce the dimension of the pressure space [20]. It should be noted that not all of these methods can meet the inf–sup condition despite alleviating volumetric locking and producing a good displacement solution. Some methods, like Q4P1, show significant oscillation for the pressure solution, known as spurious pressure mode or checkerboard mode [20]. In such cases, additional stabilization approaches, such as multi-scale stabilization (VMS) [21, 22, 23, 24] or Galerkin/least-squares (GLS) [25], are required to eliminate the oscillations in pressure.

Another class of FEM methods adjusts the constraint ratio by increasing the displacement DOFs. For instance, based on 3-node triangular elements, Arnold et al. used a cubic bubble function in each element to increase the displacement DOFs, known as the MINI element [26, 27]. It has been shown that this method belongs to the VMS framework [28], and its fulfillment of the inf–sup condition can be analytically evidenced using the two-level projection framework [7]. The Crouzeix–Raviart element [29] transfers the DOFs from the triangular vertices to edges, increasing the constraint ratio since, for triangular topology, the number of edges is greater than that of vertices. More details about FEM technology for divergence constraint issues can be found in Refs. [2, 4, 30].

In the past two decades, various novel approximations equipped with global smoothed shape functions, such as moving least-squares approximation [31], reproducing kernel approximation [32], radial basis functions [33, 34], maximum-entropy approximation [35], and NURBS approximation [36, 37], have been proposed. In these approaches, the approximant pressure evaluated by the derivatives of global continuous shape functions also maintains a constraint ratio of 2 in 2D incompressible elasticity problems. However, the corresponding results still show lower accuracy caused by locking [38, 39]. Widely-used locking-free technologies for FEM are introduced in these approaches to enhance their performance. For example, Moutsanidis et al. employed selective integration and B–bar, F–bar methods for reproducing kernel particle methods [40, 41]. Wang et al. applied selective integration schemes with bubble–stabilized functions to node–based smoothed particle FEM [42]. Elguedj et al. proposed the B–bar and F–bar NURBS formulations for linear and nonlinear incompressible elasticity. Chen et al. adopted the pressure projection approach for reproducing kernel formulations for nearly–incompressible problems [43], which was later extended to Stokes flow formulations by Goh et al. [44]. Bombarde et al. developed a block–wise NURBS formulation for shell structures, eliminating locking via

117 pressure projection [45]. Most of these approximations offer better flexibility for
118 arranging DOFs since their shape function constructions are no longer element-
119 dependent. Huerta et al. proposed a reproducing kernel approximation with
120 divergence-free basis functions to avoid volumetric strain entirely [46], although
121 this approach is unsuitable for compressible cases. Wu et al. added extra dis-
122 placement DOFs in FEM elements to resolve the locking issue, constructing
123 local shape functions using generalized meshfree interpolation to maintain con-
124 sistency [47]. Vu-Huu et al. employed different-order polygonal finite element
125 shape functions to approximate displacement and pressure, embedding a bubble
126 function in each element for stabilization.

127 This work proposes a more precise optimal divergence constraint ratio and
128 implements a locking-free mixed FEM-Meshfree formulation with this optimal
129 constraint ratio. Firstly, the inf-sup condition is derived in a new form, showing
130 that the inf-sup value equals the lowest non-zero eigenvalue of dilatation stiff-
131 ness in the context of variational analysis. Subsequently, involving a complete
132 polynomial space with dimensions identical to displacement DOFs, the num-
133 ber of non-zero eigenvalues can be analytically calculated, and a new estimator
134 considering the constraint ratio is established. From this estimator, the opti-
135 mal constraint ratio is defined with a stabilized number of pressure nodes. If
136 the constraint ratio exceeds the locking ratio, the formulation will show severe
137 locking. When the constraint ratio is lower than the optimal ratio, the formu-
138 lation achieves satisfactory results, and the inf-sup condition is fulfilled. This
139 estimator provides a strong link between the inf-sup value and the pressure
140 DOFs, making it possible to justify the locking status by counting the pressure
141 nodes. Furthermore, a mixed FEM-Meshfree formulation is proposed to verify
142 the optimal constraint ratio. In this mixed formulation, the displacement is
143 approximated by traditional finite element methods, and the pressure is dis-
144 cretized by reproducing kernel meshfree approximation. With the aid of global
145 RK shape functions, the pressure's DOFs can be adjusted arbitrarily without
146 considering approximation order and numerical integration issues to maintain-
147 ing the constraint ratio as optimal.

148 The remainder of this paper is organized as follows: Section 2 reviews the
149 mixed-formulation framework for incompressible elasticity problems. In Section
150 3, a novel estimator of the inf-sup value is developed, from which the optimal
151 constraint ratio is obtained. Section 4 introduces the mixed FEM-Meshfree
152 formulation and its corresponding nodal distribution schemes. Section 5 verifies
153 the proposed optimal constraint ratio using a set of benchmark incompressible
154 elasticity examples, studying error convergence and stability properties for the
155 mixed FEM-Meshfree approximation. Finally, the conclusions are presented in
156 Section 6.

157 **2. Mixed-formulation**

158 *2.1. Nearly-incompressible elasticity*

159 Consider a body $\Omega \in \mathbb{R}^{n_d}$ with boundary Γ in n_d -dimension, where the Γ_t
160 and Γ_g denotes its natural boundary and essential boundary such that $\Gamma_t \cup \Gamma_g =$

¹⁶¹ $\Gamma, \Gamma_t \cap \Gamma_g = \emptyset$. The corresponding governing equations for mixed-formulation
¹⁶² are given by:

$$\begin{cases} \nabla \cdot \boldsymbol{\sigma} + \mathbf{b} = \mathbf{0} & \text{in } \Omega \\ \frac{p}{\kappa} + \nabla \cdot \mathbf{u} = 0 & \text{in } \Omega \\ \boldsymbol{\sigma} \cdot \mathbf{n} = \mathbf{t} & \text{on } \Gamma_t \\ \mathbf{u} = \mathbf{g} & \text{on } \Gamma_g \end{cases} \quad (2)$$

¹⁶³ where \mathbf{u} and p , standing for displacement and hydrostatic pressure respectively,
¹⁶⁴ are the variables of this problem. $\boldsymbol{\sigma}$ denotes to stress tensor and has the following
¹⁶⁵ form:

$$\boldsymbol{\sigma}(\mathbf{u}, p) = p\mathbf{1} + 2\mu\nabla^d\mathbf{u} \quad (3)$$

¹⁶⁶ in which $\mathbf{1} = \delta_{ij}\mathbf{e}_i \otimes \mathbf{e}_j$ is second order identity tensor. $\nabla^d \cdot \mathbf{u}$ is the deviatoric
¹⁶⁷ gradient of \mathbf{u} and can be evaluated by:

$$\nabla^d\mathbf{u} = \frac{1}{2}(\mathbf{u}\nabla + \nabla\mathbf{u}) - \frac{1}{3}\nabla \cdot \mathbf{u} \quad (4)$$

¹⁶⁸ and κ, μ are the bulk modulus and shear modulus, and they can be represented
¹⁶⁹ by Young's modulus E and Poisson's ratio ν :

$$\kappa = \frac{E}{2(1-2\nu)}, \quad \mu = \frac{E}{2(1+\nu)} \quad (5)$$

¹⁷⁰ Moreover, \mathbf{b} denotes to prescribed body force in Ω . \mathbf{t}, \mathbf{g} are prescribed
¹⁷¹ traction and displacement on natural and essential boundaries respectively.

¹⁷² In accordance with Galerkin formulation, the weak form can be given by:
¹⁷³ Find $\mathbf{u} \in V, p \in Q$,

$$\begin{cases} a(\mathbf{v}, \mathbf{u}) + b(\mathbf{v}, p) = f(\mathbf{v}) & \forall \mathbf{v} \in V \\ b(\mathbf{u}, q) + c(q, p) = 0 & \forall q \in Q \end{cases} \quad (6)$$

¹⁷⁴ with the spaces V, Q defined by:

$$V = \{\mathbf{v} \in H^1(\Omega)^2 \mid \mathbf{v} = \mathbf{g}, \text{ on } \Gamma_g\} \quad (7)$$

$$Q = \{q \in L^2(\Omega) \mid \int_{\Omega} q d\Omega = 0\} \quad (8)$$

¹⁷⁶ where $a : V \times V \rightarrow \mathbb{R}$, $b : V \times Q \rightarrow \mathbb{R}$ and $c : Q \times Q \rightarrow \mathbb{R}$ are bilinear forms,
¹⁷⁷ and $f : V \rightarrow \mathbb{R}$ is the linear form. In elasticity problem, they are given by:

$$a(\mathbf{v}, \mathbf{u}) = \int_{\Omega} \nabla^d\mathbf{v} : \nabla^d\mathbf{u} d\Omega \quad (9)$$

$$b(\mathbf{v}, q) = \int_{\Omega} \nabla \cdot \mathbf{v} q d\Omega \quad (10)$$

$$c(q, p) = - \int_{\Omega} \frac{1}{3\kappa} qp d\Omega \quad (11)$$

$$f(\mathbf{v}) = \int_{\Gamma_t} \mathbf{v} \cdot \mathbf{t} d\Gamma + \int_{\Omega} \mathbf{v} \cdot \mathbf{b} d\Omega \quad (12)$$

178 2.2. Ritz–Galerkin problem and volumetric locking

179 In mixed–formulation framework, the displacement and pressure can be dis-
 180 cretized by different approximations. The approximant displacement \mathbf{u}_h and
 181 approximant pressure p_h can be expressed by:

$$\mathbf{u}_h(\mathbf{x}) = \sum_{I=1}^{n_u} N_I(\mathbf{x}) \mathbf{u}_I, \quad p_h(\mathbf{x}) = \sum_{K=1}^{n_p} \Psi_K(\mathbf{x}) p_K \quad (13)$$

182 leading these approximations into the weak form of Eq. (6) yields the following
 183 Ritz–Galerkin problems: Find $\mathbf{u}_h \in V_h$, $p_h \in Q_h$,

$$\begin{cases} a(\mathbf{v}_h, \mathbf{u}_h) + b(\mathbf{v}_h, p_h) = f(\mathbf{v}_h) & \forall \mathbf{v}_h \in V_h \\ b(\mathbf{u}_h, q_h) + c(q_h, p_h) = 0 & \forall q_h \in Q_h \end{cases} \quad (14)$$

184 For nearly incompressible material, the Poisson ratio approaches to 0.5, the
 185 bulking modulus κ will turns to be infinity based on Eq. (5). Then the bilinear
 186 form c in Eq. (11) turns to be zero. And the weak form of Eq. (14) belong to
 187 an enforcement of the volumetric strain $\nabla \cdot \mathbf{u}_h$ to be zero using the Lagrangian
 188 multiplier method, where p_h is the Lagrangian multiplier.

189 Furthermore, from the second line of Eq. (14), we have:

$$b(\mathbf{u}_h, q_h) + c(q_h, p_h) = (q_h, \nabla \cdot \mathbf{u}_h) - (q_h, \frac{1}{3\kappa} p_h) = 0, \quad \forall q_h \in Q_h \quad (15)$$

190 or

$$(q_h, 3\kappa \nabla \cdot \mathbf{u}_h - p_h) = 0, \quad \forall q_h \in Q_h \quad (16)$$

191 where (\bullet, \bullet) is the inner product operator evaluated by:

$$(q, p) := \int_{\Omega} qp d\Omega \quad (17)$$

192 Obviously in Eq. (16), p_h is the orthogonal projection of $3\kappa \nabla \cdot \mathbf{u}_h$ regarded to
 193 the space Q_h [1], and, for further development, use the nabla notion with upper
 194 tilde to name the projection operator, i.e. $p_h = \tilde{\nabla} \cdot \mathbf{u}_h$. In this circumstance,
 195 the bilinear form b in first line of Eq. (14) becomes:

$$\begin{aligned} b(\mathbf{v}_h, p_h) &= (\underbrace{\nabla \cdot \mathbf{v}_h - \tilde{\nabla} \cdot \mathbf{v}_h, p_h}_0) + (\tilde{\nabla} \cdot \mathbf{v}_h, \underbrace{p_h}_{3\kappa \tilde{\nabla} \cdot \mathbf{u}_h}) \\ &= (\tilde{\nabla} \cdot \mathbf{v}_h, 3\kappa \tilde{\nabla} \cdot \mathbf{u}_h) \\ &= \tilde{a}(\mathbf{v}_h, \mathbf{u}_h) \end{aligned} \quad (18)$$

196 where the bilinear form $\tilde{a} : V_h \times V_h \rightarrow \mathbb{R}$ is defined by:

$$\tilde{a}(\mathbf{v}_h, \mathbf{u}_h) = \int_{\Omega} 3\kappa \tilde{\nabla} \cdot \mathbf{v}_h \tilde{\nabla} \cdot \mathbf{u}_h d\Omega \quad (19)$$

197 Accordingly, the problem of Eq. (14) becomes to be one variable form: Find
198 $\mathbf{u}_h \in V_h$,

$$a(\mathbf{v}_h, \mathbf{u}_h) + \tilde{a}(\mathbf{v}_h, \mathbf{u}_h) = f(\mathbf{v}_h), \quad \forall \mathbf{v}_h \in V_h \quad (20)$$

199 As $\kappa \rightarrow \infty$, Eq. (20) can be regarded as an enforcement of volumetric strain
200 using penalty method, where \tilde{a} is the penalty term. However, it should be noted
201 that, if the mixed-formulation wants to get a satisfactory result, this orthogonal
202 projection must be surjective[48]. In the contrast of surjective case, for a given
203 $p_h \in Q_h$, it possibly cannot find a $\mathbf{u}_h \in V_h$ such that $p_h = 3\kappa \nabla \cdot \mathbf{u}_h$. It will
204 lead to a much smaller displacement than expected and an oscillated pressure
205 result. This phenomenon is so-call volumetric locking.

206 **3. Optimal volumetric constraint ratio**

207 *3.1. Inf-sup condition and its eigenvalue problem*

208 To ensure surjectivity of othogonal projection and the satisfactory result,
209 the approximations of Eq.(7) should satisfy the inf-sup condition, also known
210 as the Ladyzhenskaya–Babuška–Brezzi condition [4]:

$$\inf_{q_h \in Q_h} \sup_{\mathbf{v}_h \in V_h} \frac{|b(q_h, \mathbf{v}_h)|}{\|q_h\|_Q \|\mathbf{v}_h\|_V} \geq \beta > 0 \quad (21)$$

211 in which β , namely inf-sup value, is a constant independent of characterized
212 element size h . The norms of $\|\bullet\|_V$ and $\|\bullet\|_Q$ can be flexibly defined by:

$$\|\mathbf{v}\|_V^2 := \int_{\Omega} \nabla^s \mathbf{v} : \nabla^s \mathbf{v} d\Omega \quad (22)$$

$$\|q\|_Q^2 := \int_{\Omega} \frac{1}{3\kappa} q^2 d\Omega \quad (23)$$

213 To establish the relationship between inf-sup condition and constraint ratio,
214 the inf-sup condition is firstly transformed by the following Lemma 1:

215 **Lemma 1.** Suppose $\mathcal{P}_h : V_h \rightarrow Q_h$ is the orthogonal projection operator of
216 divergence operator $\mathcal{P} := 3\kappa \nabla \cdot$, i.e. $\mathcal{P}_h := 3\kappa \bar{\nabla} \cdot$ and satisfied Eq. (16). Such
217 that the inf-sup value can be estimated by:

$$\beta \leq \inf_{V'_h \subset V_h \setminus \ker \mathcal{P}_h} \sup_{\mathbf{v}_h \in V'_h} \frac{\|\mathcal{P}_h \mathbf{v}_h\|_Q}{\|\mathbf{v}_h\|_V} \quad (24)$$

218 in which $\ker \mathcal{P}_h \subset V$ is the kernel of \mathcal{P}_h defined by $\ker \mathcal{P}_h := \{\mathbf{v} \in V \mid \mathcal{P}_h \mathbf{v} = 0\}$.

219 PROOF. As the definition of \mathcal{P}_h , $\text{Im} \mathcal{P}_h \in Q_h$, the Eq. (21) can be rewritten as:

$$\begin{aligned} \beta &\leq \inf_{q_h \in Q_h} \sup_{\mathbf{v}_h \in V_h} \frac{|b(q_h, \mathbf{v}_h)|}{\|q_h\|_Q \|\mathbf{v}_h\|_V} = \inf_{q_h \in Q_h} \sup_{\mathbf{v}_h \in V_h} \frac{|(q_h, \frac{1}{3\kappa} \mathcal{P} \mathbf{v}_h)|}{\|q_h\|_Q \|\mathbf{v}_h\|_V} \\ &\leq \inf_{q_h \in \text{Im} \mathcal{P}_h} \sup_{\mathbf{v}_h \in V_h} \frac{|\frac{1}{3\kappa} (q_h, \mathcal{P}_h \mathbf{v}_h)|}{\|q_h\|_Q \|\mathbf{v}_h\|_V} \end{aligned} \quad (25)$$

²²⁰ For a given $q_h \in \text{Im}\mathcal{P}_h$, suppose a space $V'_h \subseteq V_h \setminus \ker P_h$ defined by:

$$V'_h = \{\mathbf{v}_h \in V_h \mid \mathcal{P}_h \mathbf{v}_h = q_h\} \quad (26)$$

²²¹ Since $\text{Im}\mathcal{P}_h \in Q_h$, in accordance with Cauchy-Schwarz inequality, we have:

$$\left| \frac{1}{3\kappa} (q_h, \mathcal{P}_h \mathbf{v}_h) \right| \leq \|q_h\|_Q \|\mathcal{P}_h \mathbf{v}_h\|_Q \quad (27)$$

²²² where this equality is holding if and only if $q_h = \mathcal{P}_h \mathbf{v}_h$, i.e.,

$$\left| \frac{1}{3\kappa} (q_h, \mathcal{P}_h \mathbf{v}_h) \right| = \|q_h\|_Q \|\mathcal{P}_h \mathbf{v}_h\|_Q, \quad \forall \mathbf{v}_h \in V'_h \quad (28)$$

²²³ And the following relationship can be evidenced:

$$\sup_{\mathbf{v}_h \in V_h} \frac{\left| \frac{1}{3\kappa} (q_h, \mathcal{P}_h \mathbf{v}_h) \right|}{\|q_h\|_Q \|\mathbf{v}_h\|_V} = \sup_{\mathbf{v}_h \in V'_h} \frac{\|\mathcal{P}_h \mathbf{v}_h\|_Q}{\|\mathbf{v}_h\|_V}, \quad \forall q_h \in \text{Im}\mathcal{P}_h \quad (29)$$

²²⁴ Consequently, with a combination of Eqs. (25) and (29), Eq. (24) can be
²²⁵ obtained.

²²⁶ **Remark 1.** With Lemma 1 and the norm definitions in Eqs. (22),(23), the
²²⁷ square of inf-sup value can further bounded by:

$$\beta^2 \leq \inf_{V'_h \subset V_h \setminus \ker \mathcal{P}_h} \sup_{\mathbf{v}_h \in V'_h} \frac{\|\mathcal{P}_h \mathbf{v}_h\|_Q^2}{\|\mathbf{v}_h\|_V^2} = \inf_{V'_h \subset V_h \setminus \ker \mathcal{P}_h} \sup_{\mathbf{v}_h \in V'_h} \frac{\tilde{a}(\mathbf{v}_h, \mathbf{v}_h)}{a(\mathbf{v}_h, \mathbf{v}_h)} \quad (30)$$

²²⁸ The left hand side of above equation is consistence with the minimum-maximum
²²⁹ principle [49] and again proof the equivalence with traditional numerical inf-sup
²³⁰ test [5]. Since that, β^2 evaluates the non-zero general eigenvalue of \tilde{a} and a in
²³¹ Eq. (20).

²³² 3.2. Inf-sup value estimator

²³³ **Theorem 1.** Suppose that P_{n_u} is a polynomial space with n_u dimensions, and
²³⁴ V_{n_u} is the polynomial displacement space, $V_{n_u} = P_{n_u}^{n_d}$. The inf-sup value β can
²³⁵ further be bounded by:

$$\beta \leq \beta_s + Ch \quad (31)$$

²³⁶ with

$$\beta_s = \inf_{V' \subset V_{n_u} \setminus \ker \mathcal{P}_h \mathcal{I}_h} \sup_{\mathbf{v} \in V'} \frac{\|\mathcal{P}\mathbf{v}\|_Q}{\|\mathbf{v}\|_V} \quad (32)$$

²³⁷ where \mathcal{I}_h is the interpolation operator of finite element approximation, corre-
²³⁸ spondingly, h is the characterized distance between control nodes.

²³⁹ PROOF. As the dimensions of V_h and V_{n_u} is identical, $\dim V_{n_u} = \dim V_h =$
²⁴⁰ $n_d \times n_u$. There exists a unique $\mathbf{v} \in V_{n_u}$ satisfying $\mathbf{v}_h = \mathcal{I}_h \mathbf{v}$. And the right side
²⁴¹ of Eq. (24) becomes:

$$\inf_{V'_h \subset V_h \setminus \ker \mathcal{P}_h} \sup_{\mathbf{v}_h \in V'_h} \frac{\|\mathcal{P}_h \mathbf{v}_h\|_Q}{\|\mathbf{v}_h\|_V} = \inf_{V' \subset V_{n_u} \setminus \ker \mathcal{P}_h \mathcal{I}_h} \sup_{\mathbf{v} \in V'} \frac{\|\mathcal{P}_h \mathcal{I}_h \mathbf{v}\|_Q}{\|\mathcal{I}_h \mathbf{v}\|_V} \quad (33)$$

²⁴² In accordance with triangular inequality, Cauchy-Schwarz inequality and the
²⁴³ relationship of Eqs. (16), we have:

$$\begin{aligned} \|\mathcal{P}_h \mathcal{I}_h \mathbf{v}\|_Q &= \sup_{q_h \in Q_h} \frac{|\frac{1}{3\kappa}(q_h, \mathcal{P}_h \mathcal{I}_h \mathbf{v})|}{\|q_h\|_Q} = \sup_{q_h \in Q_h} \frac{|(q_h, \mathcal{P} \mathcal{I}_h \mathbf{v})|}{\|q_h\|_Q} \\ &\leq \sup_{q_h \in Q_h} \frac{|(q_h, \mathcal{P} \mathbf{v})| + |(q_h, \mathcal{P} \mathbf{v} - \mathcal{P} \mathcal{I}_h \mathbf{v})|}{\|q_h\|_Q} \quad (34) \\ &\leq \|\mathcal{P} \mathbf{v}\|_Q + \|\mathcal{P}(\mathcal{I} - \mathcal{I}_h)\mathbf{v}\|_Q \end{aligned}$$

²⁴⁴ Obviously, the second term on the right side of Eq. (34) is the interpolation
²⁴⁵ error, and can be evaluated by [50]:

$$\|\mathcal{P}(\mathcal{I} - \mathcal{I}_h)\mathbf{v}\|_Q \leq Ch \|\mathbf{v}\|_V \quad (35)$$

²⁴⁶ Further leading the relation of $\|\mathcal{I}_h \mathbf{v}\|_V \geq C \|\mathbf{v}\|_V$ obtained from close graph
²⁴⁷ theorem [28] and considering Eqs. (34)-(35), the right-hand side of Eq. (33)
²⁴⁸ can be represented as:

$$\inf_{V' \subset V_{n_u} \setminus \ker \mathcal{P}_h \mathcal{I}_h} \sup_{\mathbf{v} \in V'} \frac{\|\mathcal{P}_h \mathcal{I}_h \mathbf{v}\|_Q}{\|\mathcal{I}_h \mathbf{v}\|_V} \leq \inf_{V' \subset V_{n_u} \setminus \ker \mathcal{P}_h \mathcal{I}_h} \sup_{\mathbf{v} \in V'} \frac{\|\mathcal{P} \mathbf{v}\|_Q}{\|\mathbf{v}\|_V} + Ch \quad (36)$$

²⁴⁹ Substituting Eqs. (33),(36) into (24) can finally proof the Eqs. (31), (32).

²⁵⁰ As we can see in Eqs. (31) and (32), $\beta_s \geq 0$, the β_s is equal to 0 or not
²⁵¹ determines whether the formulation can satisfy the inf-sup condition. If $\beta_s > 0$,
²⁵² as the mesh refining, the second term in the right-hand side of Eq. (31) will
²⁵³ sharply reduce and can be ignore. In contrast, if $\beta_s = 0$, the second term will
²⁵⁴ dominate, and the inf-sup condition will not be satisfied, leading to numerical
²⁵⁵ instability.

²⁵⁶ 3.3. Polynomial-wise constraint counting

²⁵⁷ From the above subsection, we can know that whether the β_s is zero or not
²⁵⁸ not determines whether the mixed-formulation can fulfill the inf-sup condition.
²⁵⁹ According to the expression of β_s in Eq. (32), as $\beta_s = 0$, the variable \mathbf{v} should
²⁶⁰ belong to $\ker \mathcal{P}$, so the dimensions of the subspace in which $\beta_s \neq 0$, namely n_s ,
²⁶¹ can be evaluated by:

$$n_s = \dim(V_{n_s} \setminus \ker \mathcal{P}) \quad (37)$$

²⁶² To further construction of the relationship between inf-sup value estimator
²⁶³ in Eq. (31) and constraint ratio $r = \frac{n_d \times n_u}{n_p}$, we should find the displacement

²⁶⁴ and pressure DOFs in Eq. (31). With the definition of V_{n_u} , the number of
²⁶⁵ displacement DOFs is easy to be evaluated by:

$$n_u = \dim V_{n_u} \quad (38)$$

²⁶⁶ With well-posed nodal distributions of displacement and pressure, the number of
²⁶⁷ pressure DOFs has the following relationship:

$$n_p = \dim Q_h = \dim(\text{Im} \mathcal{P}_h) = \dim(V_{n_u} \setminus \ker \mathcal{P}_h \mathcal{I}_h) \quad (39)$$

²⁶⁸ Fig. 1 illustrates how the relationship between n_s , n_p and n_u influence the
²⁶⁹ fulfillment of inf-sup condition:

- ²⁷⁰ As $n_p > n_s$, there must exist a subspace in space $V_{n_u} \setminus \ker \mathcal{P}_h \mathcal{I}_h$ belong to
²⁷¹ $\ker \mathcal{P}$, resulting $\beta_s = 0$, i.e. $V_{n_u} \setminus \ker \mathcal{P}_h \mathcal{I}_h \cap \ker \mathcal{P} \neq \emptyset$. At this circum-
²⁷² stance, the inf-sup condition cannot be satisfied and the formulation will
²⁷³ suffer from volumetric locking.
- ²⁷⁴ As $n_p \leq n_s$, for a well-posed nodal distributions, the space $V_{n_u} \setminus \ker \mathcal{P}_h \mathcal{I}_h$
²⁷⁵ may be a subset of $V_{n_u} \setminus \ker \mathcal{P}$. Then, the β_s will remain to be nonzero,
²⁷⁶ and the formulation will be locking-free.

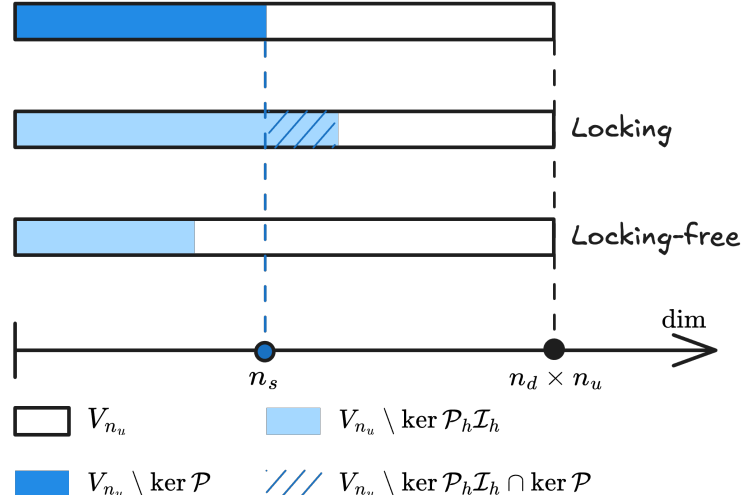


Figure 1: Illustration of estimator

²⁷⁷ Summarily, the formulation can satisfy the inf-sup condition and alleviates
²⁷⁸ the volumetric locking at least the number of pressure nodes n_p should be less
²⁷⁹ than n_s , so we name n_s as stabilized number of pressure nodes. At this moment,
²⁸⁰ the volumetric constraint ratio should meet the following relation to ensure inf-
²⁸¹ sup condition:

$$r_{opt} \geq \frac{n_d \times n_u}{n_s} \quad (40)$$

282 **Remark 2.** Some uniform element with special arrangement, like union-jack
 283 element arrangement for 3-node triangular element, can pass the inf-sup test[6],
 284 but its pressure DOFs number is greater than n_s . This is caused by that, the
 285 union-jack arrangement leads to a lower the nonzero eigenvalue number of \tilde{a}
 286 and a in Eq. (20), and the corresponding nonzero eigenvalue number is less
 287 than or equal to the stabilized number n_s , satisfying Eq. (40). The similar cases
 288 about this special element arrangement is too few, so it is more straightforward
 289 to use the number of pressure nodes n_p to measure $\dim(V_{n_u} \setminus \ker \mathcal{P}_h \mathcal{I}_h)$.

290 **Remark 3.** It is obviously that the traditional optimal constraint ratio can not
 291 fulfill this condition. However, not all formulations satisfying this condition can
 292 totally avoid volumetric locking. It is because that $n_p \leq n_s$ is not equivalent
 293 with $V_{n_u} \setminus \ker \mathcal{P}_h \mathcal{I}_h \subset V_{n_u} \setminus \ker \mathcal{P}$. Fortunately, a well-posed nodal distributions
 294 of displacement and pressure can ensure this that will be evidenced by numerical
 295 examples in the subsequent sections.

296 *3.4. Optimal volumetric constraint ratio*

297 The fulfillment of inf-sup condition should require the number of pressure
 298 nodes n_p lower than the stabilized number n_s , and now, we will demonstrate
 299 how to determine n_s for a specific number of displacement DOFs.

300 In 2D case, for instance, we first consider the linear polynomial displacement
 301 space V_3 is given by:

$$V_3 = \text{span} \left\{ \begin{pmatrix} 1 \\ 0 \end{pmatrix}, \begin{pmatrix} 0 \\ 1 \end{pmatrix}, \begin{pmatrix} x \\ 0 \end{pmatrix}, \begin{pmatrix} 0 \\ x \end{pmatrix}, \begin{pmatrix} y \\ 0 \end{pmatrix}, \begin{pmatrix} 0 \\ y \end{pmatrix} \right\} \quad (41)$$

302 or rearranged as follows,

$$V_3 = \text{span} \left\{ \underbrace{\begin{pmatrix} 1 \\ 0 \end{pmatrix}, \begin{pmatrix} 0 \\ 1 \end{pmatrix}, \begin{pmatrix} y \\ 0 \end{pmatrix}, \begin{pmatrix} 0 \\ x \end{pmatrix}, \begin{pmatrix} x \\ -y \end{pmatrix}}_{\ker \mathcal{P}}, \underbrace{\begin{pmatrix} x \\ y \end{pmatrix}}_{V_3 \setminus \ker \mathcal{P}} \right\} \quad (42)$$

303 It can be counted that, for $n_u = 3$, $n_s = 1$. Following the path, the displacement
 304 space with quadratic polynomial base namely V_6 can be stated as:

$$V_6 = \text{span} \left\{ \underbrace{\begin{pmatrix} 1 \\ 0 \end{pmatrix}, \begin{pmatrix} 0 \\ 1 \end{pmatrix}, \begin{pmatrix} y \\ 0 \end{pmatrix}, \begin{pmatrix} 0 \\ x \end{pmatrix}, \begin{pmatrix} x \\ -y \end{pmatrix}, \begin{pmatrix} x^2 \\ -2xy \end{pmatrix}, \begin{pmatrix} y^2 \\ 0 \end{pmatrix}, \begin{pmatrix} 0 \\ x^2 \end{pmatrix}, \begin{pmatrix} -2xy \\ y^2 \end{pmatrix}}_{\ker \mathcal{P}}, \underbrace{\begin{pmatrix} x \\ y \end{pmatrix}, \begin{pmatrix} x^2 \\ 2xy \end{pmatrix}, \begin{pmatrix} 2xy \\ y^2 \end{pmatrix}}_{V_6 \setminus \ker \mathcal{P}} \right\} \quad (43)$$

305 In this circumstance, $n_s = 3$. As the order of polynomial space increasing,
 306 the every optimal numbers of constraint dofs for each order of polygonal space
 307 are listed in Table. 1, in which n denotes to the order of space P_{n_u} . For the
 308 flexibility of usage, the relation between n_u and n_s is summarized as follows:

$$n_s = \frac{n(n+1)}{2}, \quad n = \left\lfloor \frac{\sqrt{1+8n_u} - 3}{2} \right\rfloor \quad (44)$$

Table 1: Relationship between displacement DOFs and stabilized number

n	2D		3D	
	n_u	n_s	n_u	n_s
1	3	1	4	1
2	6	3	10	4
3	10	6	20	10
4	15	10	35	20
\vdots	\vdots	\vdots	\vdots	\vdots

For 3D case, following the path in 2D, the lienar polynomial space V_4 is considered herein, and the arranged space of V_4 is listed as follows:

$$V_4 = \text{span} \left\{ \underbrace{\begin{pmatrix} 1 \\ 0 \\ 0 \end{pmatrix}, \begin{pmatrix} 0 \\ 1 \\ 0 \end{pmatrix}, \begin{pmatrix} 0 \\ 0 \\ 1 \end{pmatrix}, \begin{pmatrix} 0 \\ x \\ 0 \end{pmatrix}, \begin{pmatrix} 0 \\ 0 \\ x \end{pmatrix}, \begin{pmatrix} y \\ 0 \\ 0 \end{pmatrix}}_{\ker \mathcal{P}}, \underbrace{\begin{pmatrix} 0 \\ y \\ 0 \end{pmatrix}, \begin{pmatrix} z \\ 0 \\ 0 \end{pmatrix}, \begin{pmatrix} 0 \\ z \\ 0 \end{pmatrix}, \begin{pmatrix} x \\ -y \\ 0 \end{pmatrix}, \begin{pmatrix} x \\ 0 \\ -z \end{pmatrix}, \begin{pmatrix} y \\ z \\ 0 \end{pmatrix}}_{V_{n_u} \setminus \ker \mathcal{P}} \right\} \quad (45)$$

For brevity, the stabilized numbers for higher order polynomial displacement space is directly listed in Table. 1, and it can be summarized that, for a given number of displacement DOFs, the stabilized number for pressure DOFs can be calculated as follows:

$$n_s = \frac{n(n+1)(n+2)}{6} \quad (46)$$

$$n = \left\lfloor \left(3n_u + \frac{1}{3} \sqrt{81n_u^2 - \frac{1}{3}} \right)^{\frac{1}{3}} + \frac{1}{3 \left(3n_u + \frac{1}{3} \sqrt{81n_u^2 - \frac{1}{3}} \right)^{\frac{1}{3}}} - 2 \right\rfloor \quad (47)$$

Table 2: Inf-sup condition for various mixed formulations

Formulation	Constraint Ratio $r > n_d$	Inf-sup condition		Constraint Ratio $r = r_{opt}$
		Numerical	Analytical	
T3P1($r = 1$)	✗	✗	✗	✗
Q4P1($r = 2$)	✓	✗	✗	✗

³¹⁵ **4. FE–Meshfree mixed formulation with optimal constraint**

³¹⁶ In the proposed mixed-formulation, the displacement is approximated using
³¹⁷ three-node, six-node triangular elements and four-node, eight-node quadrilateral
³¹⁸ elements [2]. In order to flexcially adjust to let the dofs of pressure meets
³¹⁹ to be optimal, the reproducing kernel meshfree approximation is involved to
³²⁰ approximate pressure.

³²¹ *4.1. Reproducing kernel meshfree approximation*

³²² In accordance with the reproducing kernel approximation, the entire domain
³²³ Ω is discretized by n_p meshfree nodes, $\{\mathbf{x}_I\}_{I=1}^{n_p}$. The approximated pressure
³²⁴ namely p_h can be expressed by shape function Ψ_I and nodal coefficient p_I ,
³²⁵ yields:

$$p_h(\mathbf{x}) = \sum_{I=1}^{n_p} \Psi_I(\mathbf{x}) p_I \quad (48)$$

³²⁶ where, in the reproducing kernel approximation framework, the shape function
³²⁷ Ψ_I is given by:

$$\Psi_I(\mathbf{x}) = \mathbf{c}(\mathbf{x}_I - \mathbf{x}) \mathbf{p}(\mathbf{x}_I - \mathbf{x}) \phi(\mathbf{x}_I - \mathbf{x}) \quad (49)$$

³²⁸ in which \mathbf{p} is the basis function, especially for 2D quadratic basis function,
³²⁹ having the following form:

$$\mathbf{p}(\mathbf{x}) = \{1, x, y, x^2, xy, y^2\}^T \quad (50)$$

³³⁰ and ϕ stands for the kernel function. In this work, the traditional Cubic B-spline
³³¹ function with square support is used as the kernel function:

$$\phi(\mathbf{x}_I - \mathbf{x}) = \phi(s_x) \phi(s_y), \quad s_i = \frac{\|\mathbf{x}_I - \mathbf{x}\|}{\bar{s}_{iI}} \quad (51)$$

³³² with

$$\phi(s) = \frac{1}{3!} \begin{cases} (2-2s)^3 - 4(1-2s)^3 & s \leq \frac{1}{2} \\ (2-2s)^3 & \frac{1}{2} < s < 1 \\ 0 & s > 1 \end{cases} \quad (52)$$

³³³ where \bar{s}_{iI} 's are the support size towards the i -direction for the shape function Ψ_I .
³³⁴ The correction function \mathbf{c} can be determined by the following so-call consistency
³³⁵ condition:

$$\sum_{I=1}^{n_p} \Psi_I(\mathbf{x}) \mathbf{p}(\mathbf{x}_I) = \mathbf{p}(\mathbf{x}) \quad (53)$$

³³⁶ or equivalent shifted form:

$$\sum_{I=1}^{n_p} \Psi_I(\mathbf{x}) \mathbf{p}(\mathbf{x}_I - \mathbf{x}) = \mathbf{p}(\mathbf{0}) \quad (54)$$

³³⁷ Substituting Eq. 49 into Eq. (54) leads to:

$$\mathbf{c}(\mathbf{x}_I - \mathbf{x}) = \mathbf{A}^{-1}(\mathbf{x}_I - \mathbf{x}) \mathbf{p}(\mathbf{0}) \quad (55)$$

³³⁸ in which \mathbf{A} is namely moment matrix evaluating by:

$$\mathbf{A}(\mathbf{x}_I - \mathbf{x}) = \sum_{I=1}^{n_p} \mathbf{p}(\mathbf{x}_I - \mathbf{x}) \mathbf{p}^T(\mathbf{x}_I - \mathbf{x}) \phi(\mathbf{x}_I - \mathbf{x}) \quad (56)$$

³³⁹ Taking Eq. (55) back to Eq. (49), the final form of reproducing kernel shape
³⁴⁰ function can be got as:

$$\Psi_I(\mathbf{x}) = \mathbf{p}^T(\mathbf{0}) \mathbf{A}^{-1}(\mathbf{x}_I - \mathbf{x}) \phi(\mathbf{x}_I - \mathbf{x}) \quad (57)$$

³⁴¹ 4.2. Optimal pressure nodes distributions

³⁴² In this subsection, the 2D and 3D inf-sup tests [6] with the FE-meshfree
³⁴³ mixed formulation is employed to validate of the proposed estimator of inf-sup
³⁴⁴ value. The 2D test considers the square domain $\Omega = (0, 1) \otimes (0, 1)$ in Fig.
³⁴⁵ 3, where the displacement is discretized by linear Triangular element (Tri3),
³⁴⁶ Quadrilateral element (Quad4) with 4×4 , 8×8 , 16×16 and 32×32 elements,
³⁴⁷ quadratic Triangular element (Tri6), Quadrilateral element (Quad8) with 2×2 ,
³⁴⁸ 4×4 , 8×8 and 16×16 elements, respectively. The 3D test employs a cube
³⁴⁹ domain $\Omega = (0, 1) \otimes (0, 1) \otimes (0, 1)$ in Fig. 4 with 4×4 , 8×8 and 16×16
³⁵⁰ elements for the 4-node tetrahedral element (Tet4) and 8-node hexahedral ele-
³⁵¹ ment (Hex8). In order to avoid the influence of interpolation error, the uniform
³⁵² nodal distributions are used for pressure discretizations.

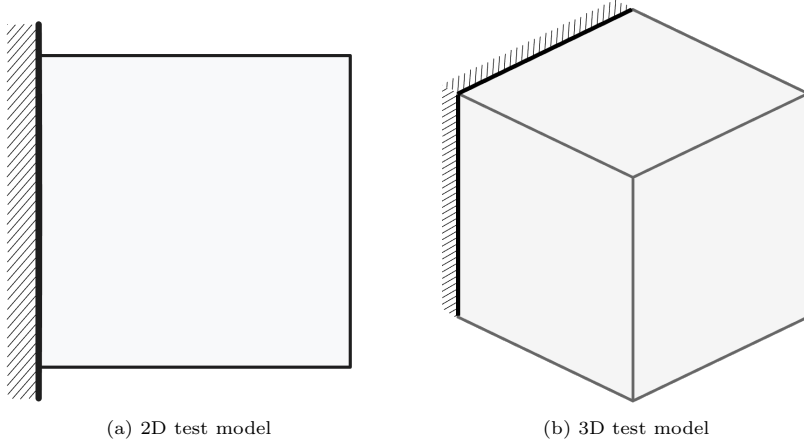


Figure 2: Illustration of inf-sup test

353 Figures 3 and 4 show the corresponding results, in which the red line stands
 354 for the value of β respected to the number of pressure nodes n_p , the vertical dash
 355 line denotes to the stabilized number n_s . The deeper color of lines means the
 356 mesh refining. The results show that, no matter linear or quadratic elements,
 357 as n_p increases over the n_s , the β 's value sharply decrease, and then the inf-sup
 358 condition cannot be maintained. This result is consistent with the discussion in
 359 Section 3, and again verify the effect of the proposed estimator.

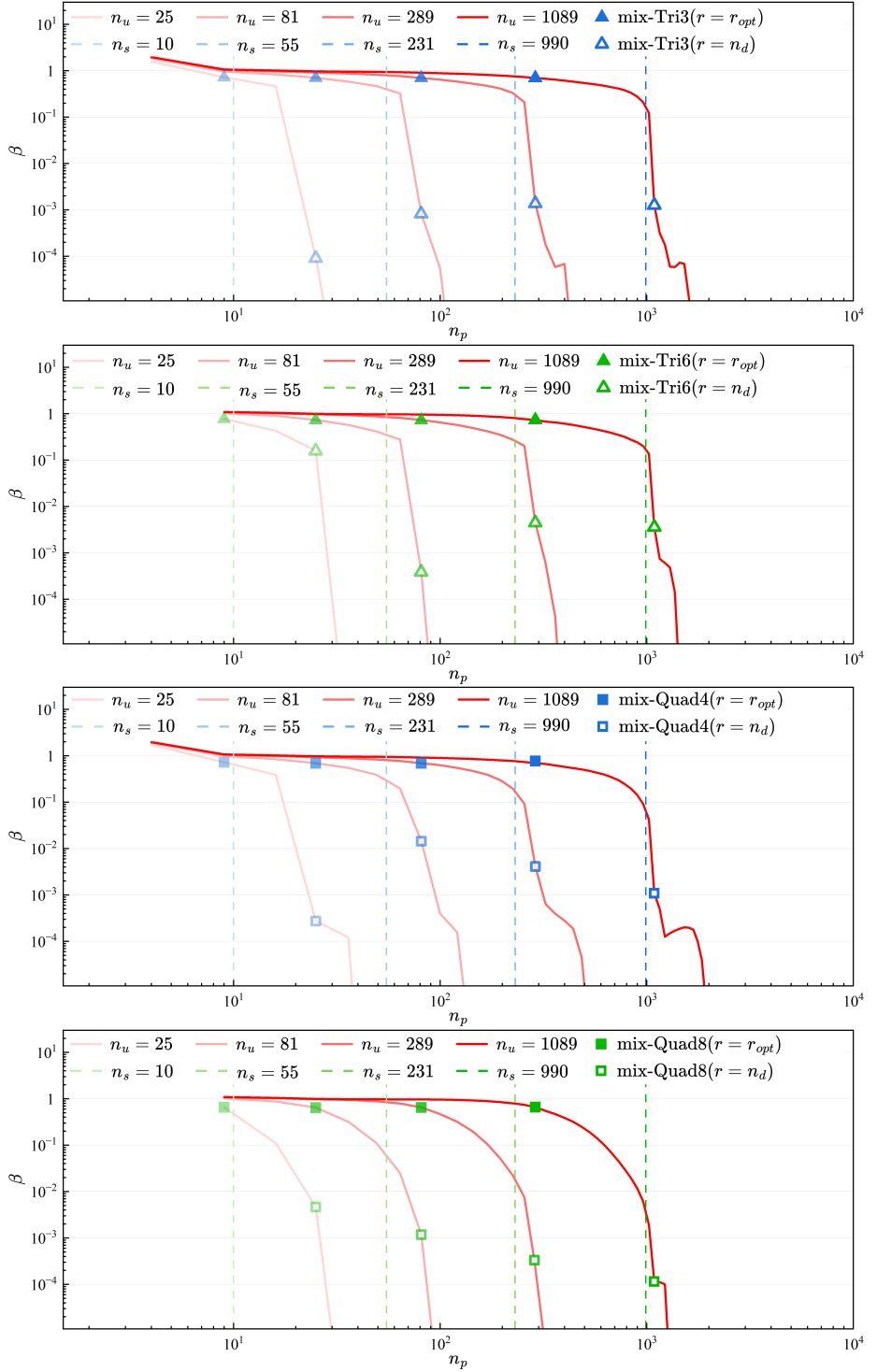


Figure 3: Inf-sup test for 2D mixed FE-meshfree formulations:
(a) mix-Tri3; (b) mix-Tri6; (c) mix-Quad4; (d) mix-Quad8

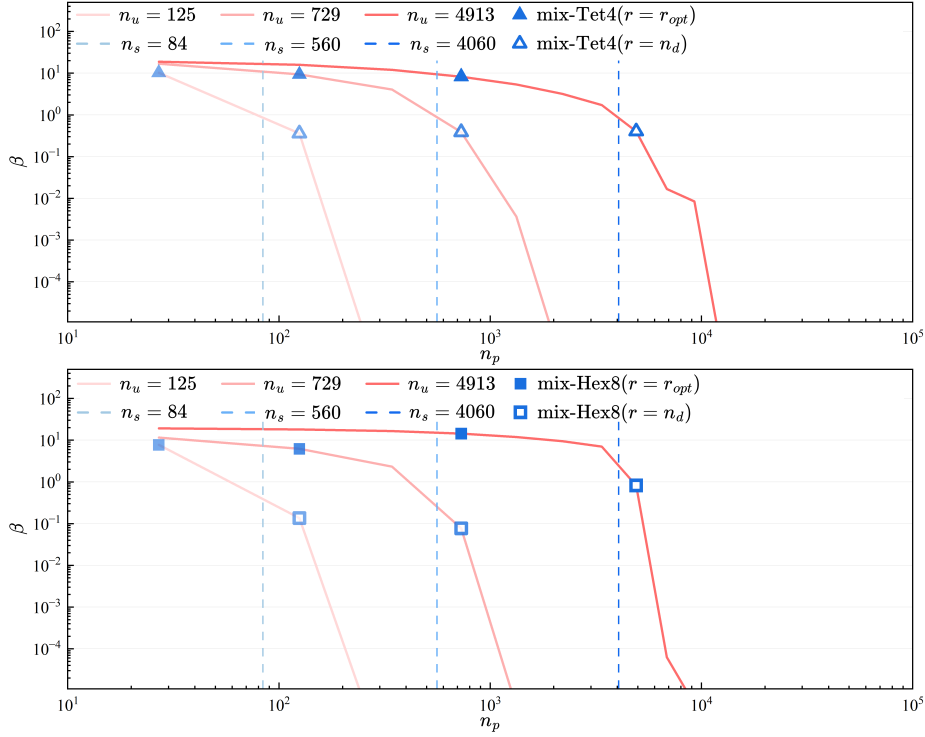


Figure 4: Inf-sup test for 3D mixed FE-meshfree formulations:
 (a) mix-Tet4; (b) mix-Hex8

Moreover, the mixed formulation's results with traditional optimal constraint ratio $r = n_d$ are listed in 3 as well, and the β in this circumstance is already much smaller than those in optimal range. Considering the results shown above, the easy-programming and efficiency, the pressure nodes are chosen among the displacement nodes. The final schemes for linear and quadratic, 2D and 3D elements discretizations are shown in Figure 5, in which all constraint ratios are belong to the range of optimal ratio. The corresponding inf-sup test results for these schemes also be marked in Figure 2 and show that, with the mesh refining, their β 's are always maintained in a non-negligible level.

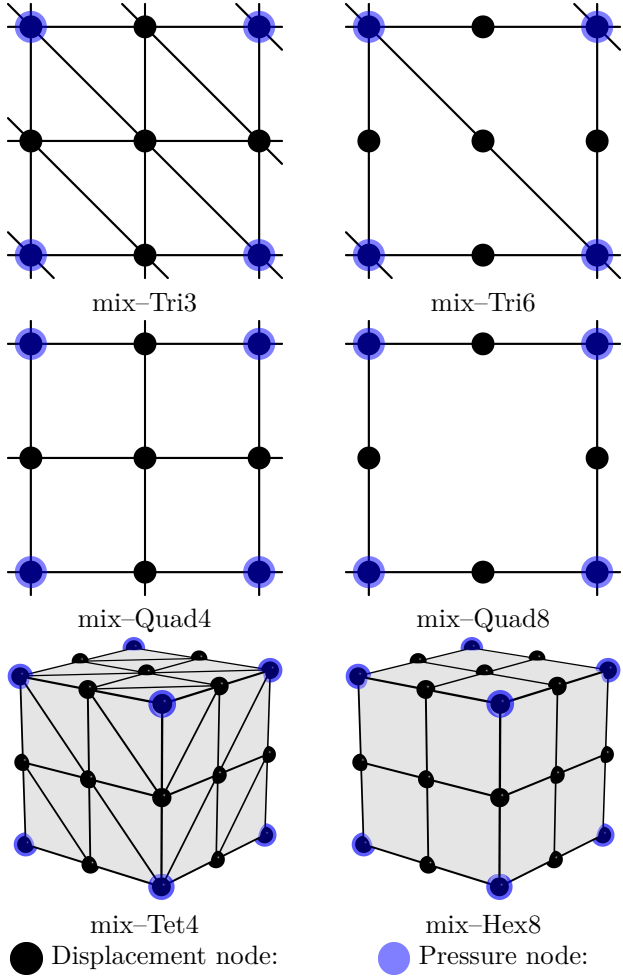


Figure 5: Nodal distribution schemes for FE-MF mixed formulations with $r = r_{opt}$

369 **5. Numerical examples**

370 **5.1. Cantilever beam problem**

371 Consider the cantilever beam problem shown in Figure 6 with length $L = 48$,
 372 width $D = 12$, and the incompressible material parameters are employed with
 373 Young's modulus $E = 3 \times 10^6$, Poisson's ratio $\nu = 0.5 - 10^{-8}$. The left hand
 374 side is fixed and the right side subject a concentrate force $P = 1000$. All the
 375 prescribed values in boundary conditions are evaluated by analytical solution

³⁷⁶ that is given as follows[51]:

$$\begin{cases} u_x(\mathbf{x}) = -\frac{Py}{6\bar{E}I} \left((6L - 3x)x + (2 + \bar{\nu})(y^2 - \frac{D^2}{4}) \right) \\ u_y(\mathbf{x}) = \frac{Py}{6\bar{E}I} \left(3\bar{\nu}y^2(L - x) + (4 + 5\bar{\nu})\frac{D^2x}{4} + (3L - x)x^2 \right) \end{cases} \quad (58)$$

³⁷⁷ where I is the beam's moment of inertia, \bar{E} and $\bar{\nu}$ are the material parameters
³⁷⁸ for plane strain hypothesis, they can be expressed by:

$$I = \frac{D^3}{12}, \quad \bar{E} = \frac{E}{1 - \nu^2}, \quad \bar{\nu} = \frac{\nu}{1 - \nu} \quad (59)$$

³⁷⁹ And correspondingly, the stress components are evaluated by

$$\begin{cases} \sigma_{xx} = -\frac{P(L - x)y}{I} \\ \sigma_{yy} = 0 \\ \sigma_{xy} = \frac{P}{2I} \left(\frac{D^2}{4} - y^2 \right) \end{cases} \quad (60)$$

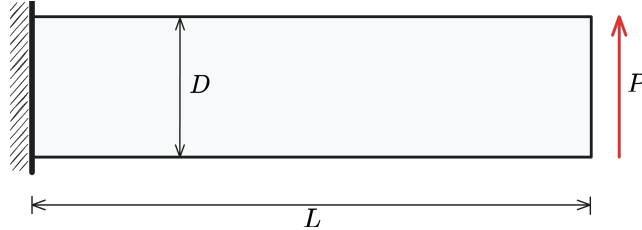


Figure 6: Illustration of cantilever beam problem

³⁸⁰ In this problem, the Quad4 element with 16×4 , 32×8 , 64×16 , 128×32
³⁸¹ grids, and Quad8 element with 8×2 , 16×4 , 32×8 , 64×16 grids are em-
³⁸² ployed for displacement discretization. The pressure are discretized by linear
³⁸³ and quadratic meshfree approximations with 1.5 and 2.5 characterized support
³⁸⁴ sizes respectively. The strain and pressure errors respected to pressure nodes
³⁸⁵ n_p are displayed in Figure 7, where the vertical dashed lines stand for the stabi-
³⁸⁶ lized number n_s . The figure implies that, the Quad8 shows better performance
³⁸⁷ than Quad4, since the Quad8's displacement results are stable no matter the
³⁸⁸ constraint ratio in optimal range or not. And the Quad4's displacement errors
³⁸⁹ increase as soon as the $n_p > n_s$. However, both Quad4's and Quad8's pres-
³⁹⁰ sure error immediately increase while their constraint ratios are out of optimal
³⁹¹ range, and Quad8 still have better results than Quad4. Figure 8 is the strain
³⁹² and pressure error convergence comparisons for this cantilever beam problem,
³⁹³ in which, except Quad8-RK($r = 2$) for strain error, all formulations with tra-
³⁹⁴ ditional constraint ratio of $r = 2$ cannot ensure the optimal error convergence

³⁹⁵ rates. The proposed mixed formulations with $r = r_{opt}$ can maintain the optimal
³⁹⁶ error convergence ratio and show a better accuracy.

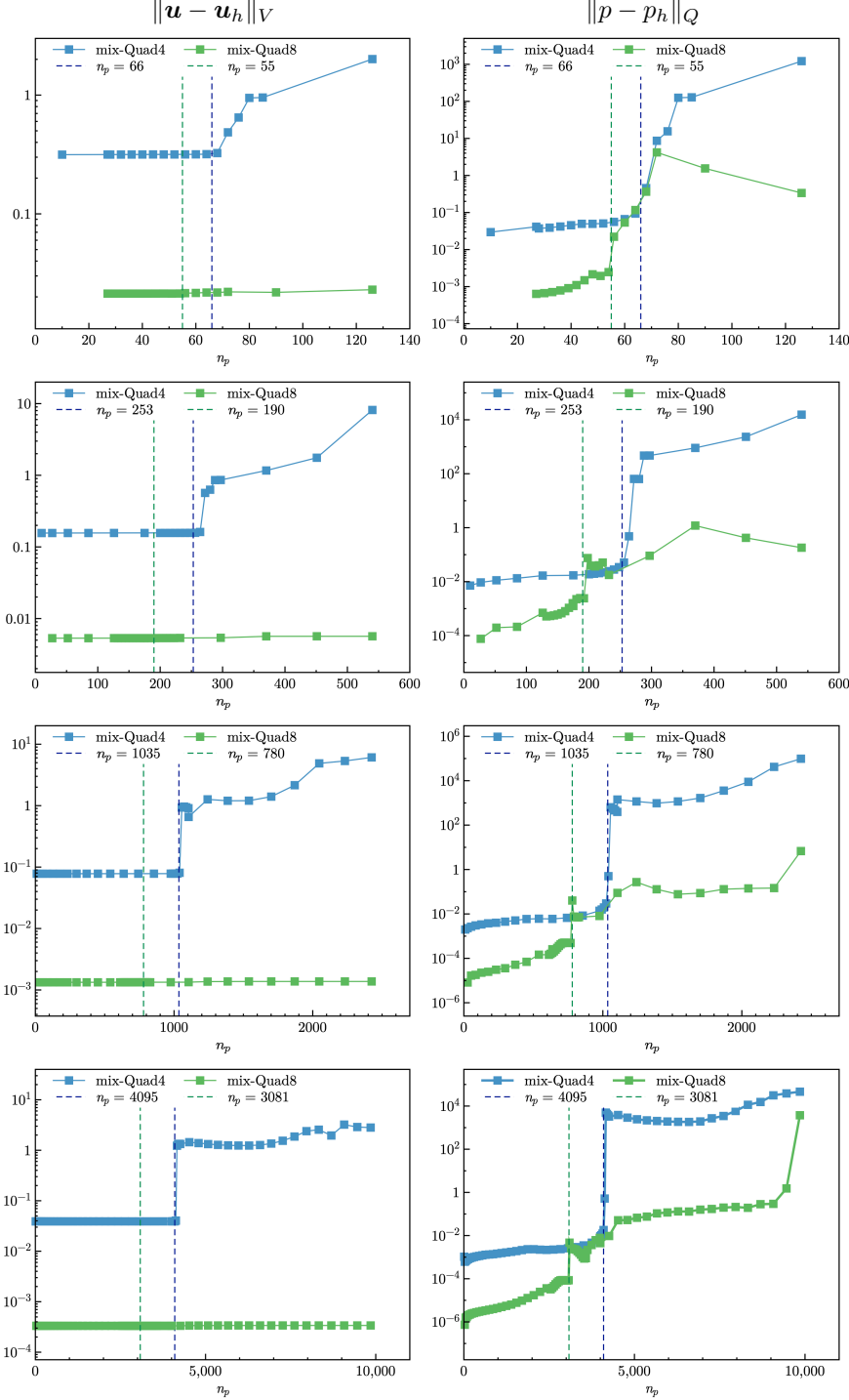


Figure 7: Strain and pressures errors v.s. n_p for cantilever beam problem

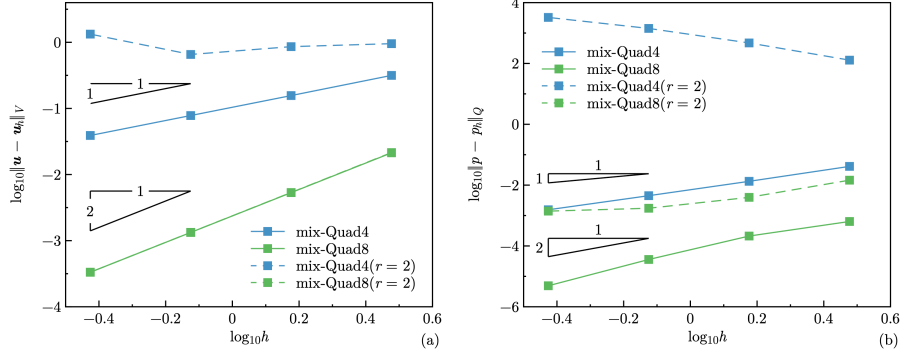


Figure 8: Error convergence study for cantilever beam problem: (a) Strain, (b) Pressure

397 5.2. Plate with hole problem

398 Consider an infinite plate with a hole centered at the origin, as shown in
399 Figure 9, and at the infinity towards x -direction subjected an uniform traction
400 $T = 1000$. The geometric and material parameters for this problem is that
401 the ratio of the hole $a = 1$, Young's modulus $E = 3 \times 10^6$ and Poisson's ratio
402 $\nu = 0.5 - 10^{-8}$. The analytical solution of this problem refers the Michell
403 solution [51] as:

$$\begin{cases} u_x(\rho, \theta) = \frac{T a}{8\mu} \left(\frac{\rho}{a} (k+1) \cos \theta - \frac{2a^3}{\rho^3} \cos 3\theta + \frac{2a}{\rho} ((1+k) \cos \theta + \cos 3\theta) \right) \\ u_y(\rho, \theta) = \frac{T a}{8\mu} \left(\frac{\rho}{a} (k-3) \sin \theta - \frac{2a^3}{\rho^3} \sin 3\theta + \frac{2a}{\rho} ((1-k) \sin \theta + \sin 3\theta) \right) \end{cases} \quad (61)$$

404 in which $k = \frac{3-\nu}{1+\nu}$, $\mu = \frac{E}{2(1+\nu)}$. And the stress components are given by:

$$\begin{cases} \sigma_{xx} = T \left(1 - \frac{a^2}{\rho^2} \left(\frac{3}{2} \cos 2\theta + \cos 4\theta \right) + \frac{3a^4}{2\rho^4} \cos 4\theta \right) \\ \sigma_{yy} = -T \left(\frac{a^2}{\rho^2} \left(\frac{1}{2} \cos 2\theta - \cos 4\theta \right) + \frac{3a^4}{2\rho^4} \cos 4\theta \right) \\ \sigma_{xy} = -T \left(\frac{a^2}{\rho^2} \left(\frac{1}{2} \sin 2\theta + \sin 4\theta \right) - \frac{3a^4}{2\rho^4} \sin 4\theta \right) \end{cases} \quad (62)$$

405 According to the symmetry property of this problem, only quarter model
406 with length $b = 5$ is considered as shown in Figure 9. The displacement is
407 discretized by 3-node and 6-node triangular elements with 81, 299, 1089 and
408 4225 nodes. The corresponding linear and quadratic meshfree formulations are
409 employed for pressure discretization, and the characterized support sizes are
410 chosen as 1.5 and 2.5 respectively. Figure 10 studies the relationship between
411 strain, pressure errors and n_p , unlike the quadrilateral element case in Section
412 5.1, the quadratic Tri6-RK shows worse results while the constraint ratio out
413 of the optimal range. And Tri3-RK exhibits less sensitivity in strain error than

414 Tri6–RK, but its error is increasing while the n_p goes up. Both Tri3–RK and
 415 Tri6–RK with constraint ratio under optimal range performance an acceptable
 416 result. The corresponding error convergence study is presented in Figure 11,
 417 only Tri3–RK with $r = 2$ shows a comparable result with the optimal one with
 418 $r = r_{opt}$, the other formulations with traditional constraint ratio show lower
 419 accuracy and error convergence rate.

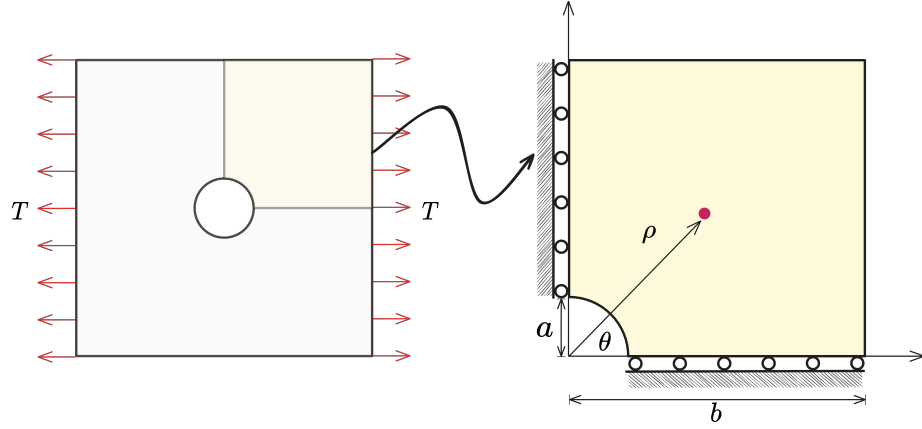


Figure 9: Illustration of plate with hole problem

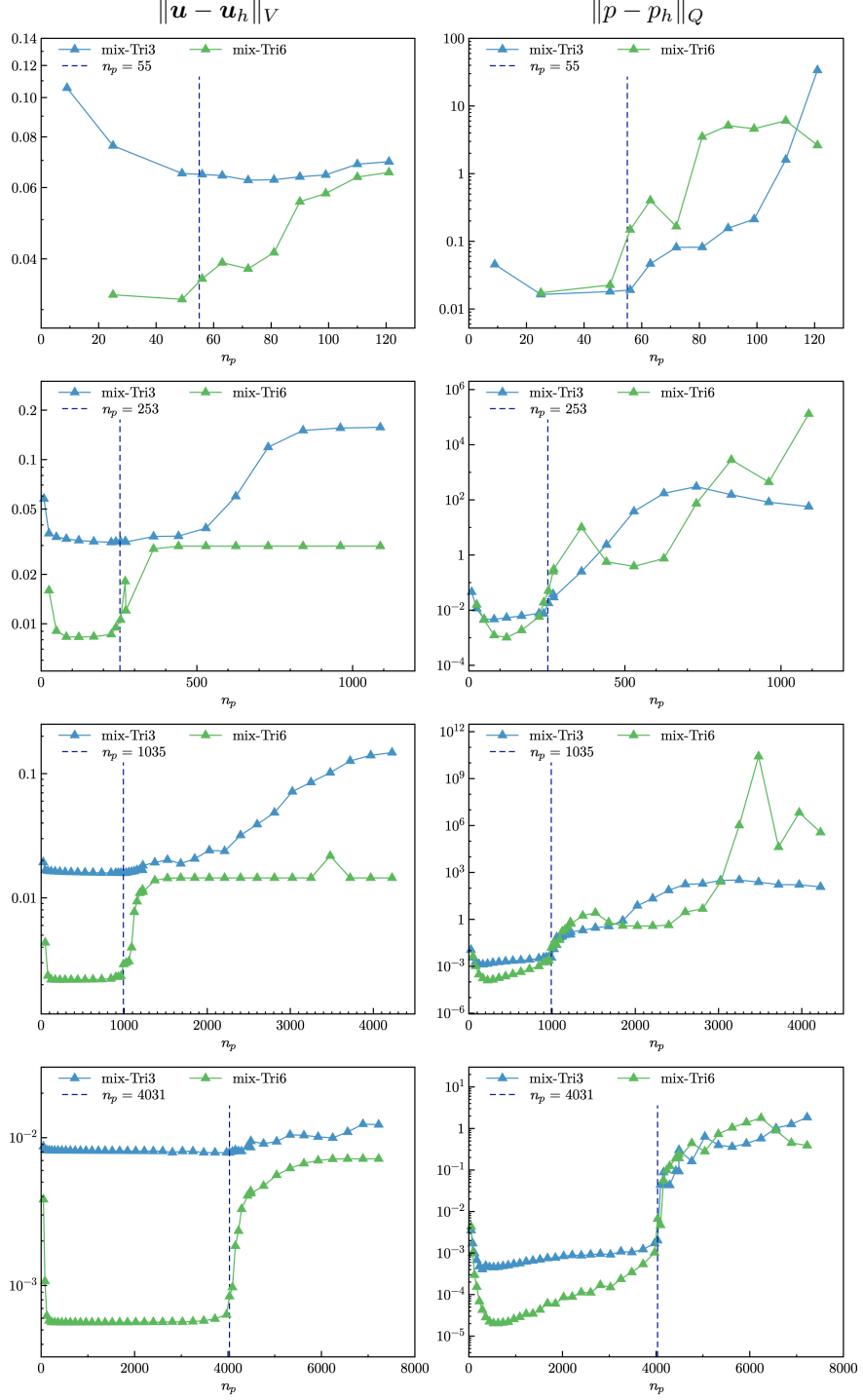


Figure 10: Strain and pressures errors v.s. n_p for plate with hole problem

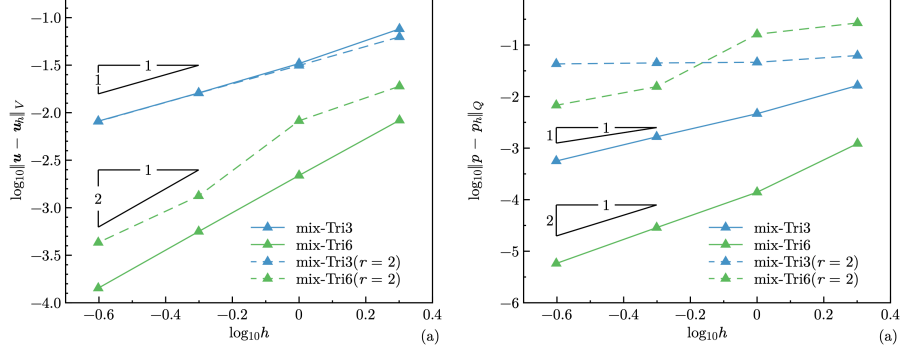


Figure 11: Error convergence study for plate with a hole problem: (a) Strain, (b) Pressure

420 5.3. Cook membrane problem

421 The cook membrane problem [12] is used herein for stability analysis of
 422 pressure. The geometry of this problem is shown in Figure 12, in which the left
 423 hand side is fixed and the right hand side subjects a concentrated force $P = 1000$
 424 in y -direction. The material parameters are Young's modulus $E = 3 \times 10^6$ and
 425 Poisson's ratio $\nu = 0.5 - 10^{-8}$.

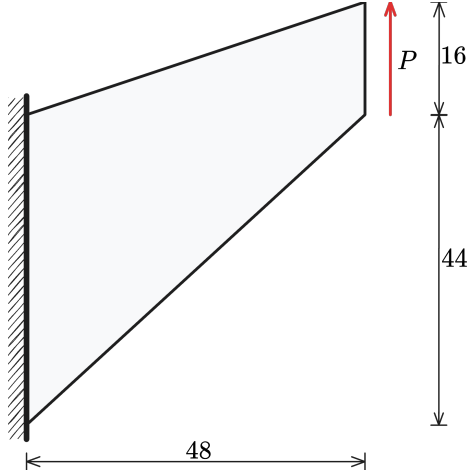


Figure 12: Illustration of cook membrane problem

426 In this test, we focus on the pressure stability of 2D mixed FE–meshfree for-
 427 mulations, the Figures 13–16 show the pressure contour plots for non-uniform
 428 Tri3–RK, Tri6–RK, Quad4–RK and Quad8–RK formulations with $r = n_d$ and
 429 $r = r_{opt}$, respectively. The reproducing kernel meshfree approximations are em-
 430 ployed for pressure discretization with characterized support sizes of 1.5 for
 431 linear basis function and 2.5 for quadratic basis function. The results imply
 432 that the pressure contour plots with the optimal constraint ratio $r = r_{opt}$ show

⁴³³ a more stable and smooth pressure distribution compared to those with the
⁴³⁴ traditional constraint ratio $r = n_d$.

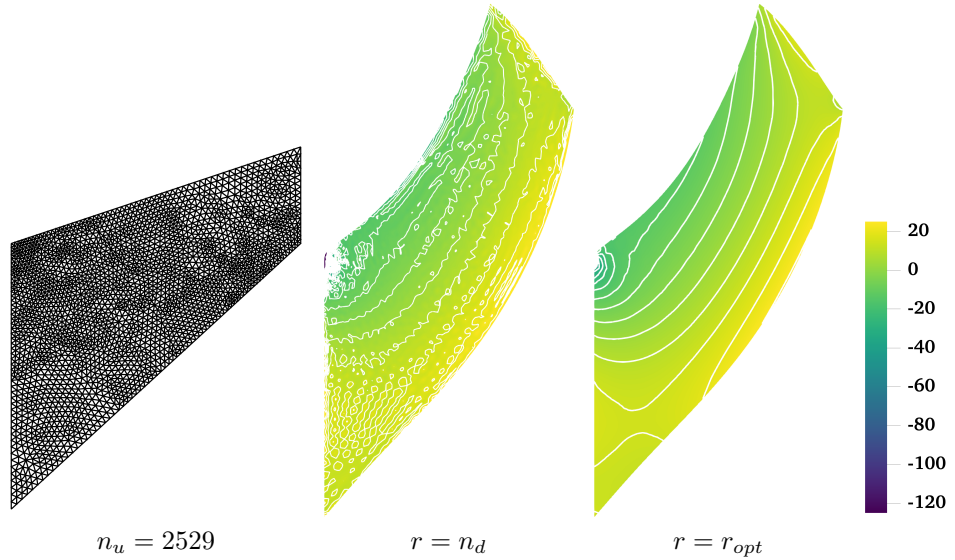


Figure 13: Comparison of pressure contour plots for cook membrane problem with Tri3–RK

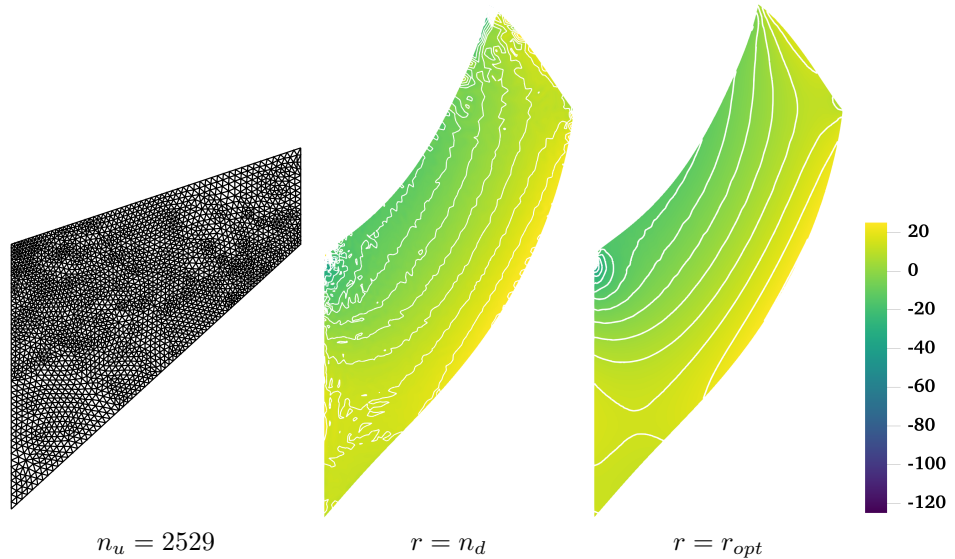


Figure 14: Comparison of pressure contour plots for cook membrane problem with Tri6–RK

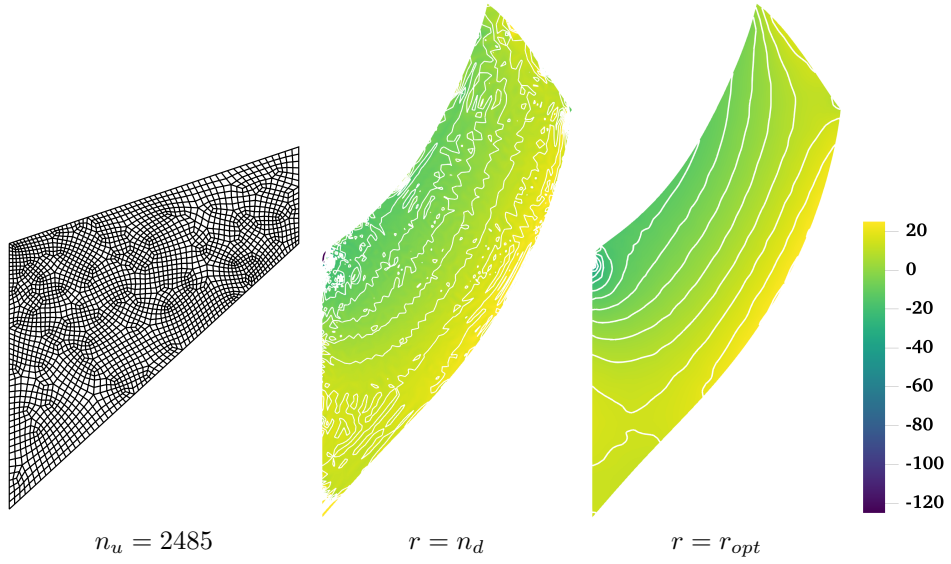


Figure 15: Comparison of pressure contour plots for cook membrane problem with Quad4–RK

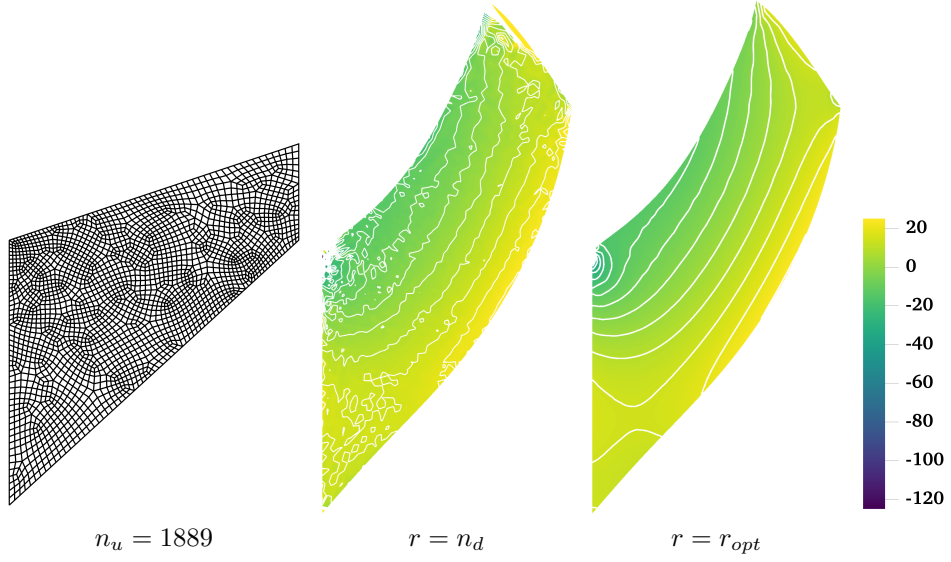


Figure 16: Comparison of pressure contour plots for cook membrane problem with Quad8–RK

435 *5.4. Block with pressure problem*

436 The incompressible block problem shown in Figure 17 is considered for test-
437 ing 3D mixed formulations, the block’s dimensions are $2L \times 2L \times L$, $L = 1$. At
438 the center of the top surface of the block is applied a pressure load $P = 1$ with

439 the area of $L \times L$. Due to the symmetry of this problem, only quarter model
 440 is considered. The Young's modulus and Poisson's ratio are set as $E = 3 \times 10^6$
 441 and $\nu = 0.5 - 10^{-8}$, respectively.

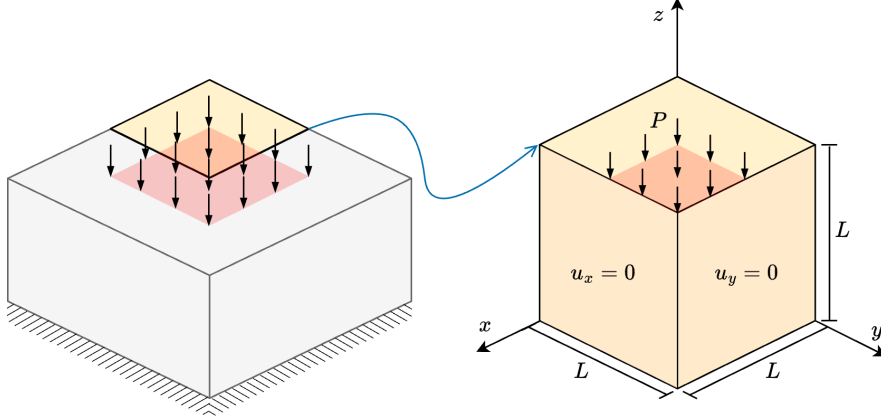


Figure 17: Illustration of block under compression problem

442 Figures study the pressure stability of 3D mixed FE-meshfree formulations,
 443 Tet4-RK and Hex8-RK, with non-uniform nodal distribution, while the pres-
 444 sure discretized by linear meshfree approximations with characterized support
 445 size of 1.5. The corresponding results also show the well performance of the
 446 proposed optimal constraint ratio $r = r_{opt}$. The mixed formulations with tra-
 447 ditional constraint ratio $r = n_d$ show a comparable displacement results, but
 448 exhibit a significant pressure instability.

449 6. Conclusion

450 This paper proposes a novel optimal constraint ratio derived from the inf-sup
 451 condition to address volumetric locking. The optimal constraint ratio requires
 452 that, for a given number of displacement DOFs, the number of pressure DOFs
 453 should remains below a stabilized number determined by the proposed inf-sup
 454 value estimator. For a well-posed nodal distribution, simply counting the dis-
 455 placement and pressure DOFs can determine whether the formulation satisfies
 456 the inf-sup condition. Compared to the traditional constraint ratio, the pro-
 457 posed ratio is theoretically grounded in the inf-sup condition and thus is more
 458 precise.

459 To implement this constraint ratio, a mixed finite element (FE) and meshfree
 460 formulation is developed. Displacements are discretized using 3-node and 6-
 461 node triangular elements, 4-node and 8-node quadrilateral elements in 2D, and
 462 4-node tetrahedral and 8-node hexahedral elements in 3D. Correspondingly,
 463 linear and quadratic reproducing kernel meshfree approximations are used for
 464 pressure discretization. The reproducing kernel approximation equips globally

465 smooth shape functions, allowing arbitrary pressure DOF placement without
466 the limit of element.

467 Inf-sup tests for mixed FE-meshfree formulations with different constraint
468 ratios verify the effectiveness of the proposed inf-sup value estimator. For effi-
469 ciency and ease of implementation, the final nodal distribution scheme selects
470 every other displacement node as a pressure node, ensuring the optimal con-
471 straint ratio and satisfying the inf-sup condition.

472 A series of 2D and 3D incompressible elasticity examples demonstrate the
473 effectiveness of the proposed mixed formulation. Results show that formulations
474 with the optimal constraint ratio yield accurate displacement and pressure solu-
475 tions. When the constraint ratio exceeds the optimal value, errors rise sharply
476 to unacceptable levels, with the 8-node quadrilateral element being the only
477 exception that maintains good displacement accuracy. Error convergence stud-
478 ies and pressure contour plots further confirm that mixed formulations with
479 the optimal constraint ratio achieve optimal convergence rates and effectively
480 suppress pressure oscillations.

481 **References**

- 482 [1] F. Brezzi, M. Fortin, Mixed and Hybrid Finite Element Methods, Vol. 15 of
483 Springer Series in Computational Mathematics, Springer, New York, NY,
484 1991.
- 485 [2] T. J. Hughes, The Finite Element Method: Linear Static and Dynamic
486 Finite Element Analysis, Prentice Hall, New Jersey, 2000.
- 487 [3] I. Babuška, R. Narasimhan, The Babuška-Brezzi condition and the patch
488 test: An example, Computer Methods in Applied Mechanics and Engineering
489 140 (1997) 183–199.
- 490 [4] K. J. Bathe, Finite Element Procedures, Prentice Hall, Englewood Cliffs,
491 New Jersey, 1996.
- 492 [5] D. S. Malkus, Eigenproblems associated with the discrete LBB condition for
493 incompressible finite elements, International Journal of Engineering Science
494 19 (1981) 1299–1310.
- 495 [6] D. Chapelle, K. J. Bathe, The inf-sup test, Computers & Structures 47
496 (1993) 537–545.
- 497 [7] F. Brezzi, K. J. Bathe, Studies of finite element procedures the inf-sup
498 condition equivalent forms and applications.
- 499 [8] D. Gallistl, Rayleigh-Ritz approximation of the inf-sup constant for the
500 divergence, Mathematics of Computation 88 (2019) 73–89.
- 501 [9] P. Hood, C. Taylor, Navier-Stokes equations using mixed interpolation,
502 Finite element methods in flow problems (1974) 121–132.

- 503 [10] D. S. Malkus, T. J. Hughes, Mixed finite element methods - Reduced and
 504 selective integration techniques: A unification of concepts, Computer Meth-
 505 ods in Applied Mechanics and Engineering 15 (1978) 63–81.
- 506 [11] T. Shilt, R. Deshmukh, J. J. McNamara, P. J. O'Hara, Solution of nearly
 507 incompressible field problems using a generalized finite element approach,
 508 Computer Methods in Applied Mechanics and Engineering 368 (2020)
 509 113165.
- 510 [12] J. C. Simo, M. S. Rifai, A class of mixed assumed strain methods and
 511 the method of incompatible modes, International Journal for Numerical
 512 Methods in Engineering 29 (1990) 1595–1638.
- 513 [13] M. Broccardo, M. Micheloni, P. Krysl, Assumed-deformation gradient finite
 514 elements with nodal integration for nearly incompressible large deformation
 515 analysis, International Journal for Numerical Methods in Engineering 78
 516 (2009) 1113–1134.
- 517 [14] W. M. Coombs, T. J. Charlton, M. Cortis, C. E. Augarde, Overcoming vol-
 518 umetric locking in material point methods, Computer Methods in Applied
 519 Mechanics and Engineering 333 (2018) 1–21.
- 520 [15] S. Saloustros, M. Cervera, S. Kim, M. Chiumenti, Accurate and locking-free
 521 analysis of beams, plates and shells using solid elements, Computational
 522 Mechanics (Jan. 2021).
- 523 [16] C. Rodriguez, T.-H. Huang, A variationally consistent reproducing ker-
 524 nel enhanced material point method and its applications to incompressible
 525 materials, Computational Mechanics (2023) 1–20.
- 526 [17] J. Simo, R. Taylor, K. Pister, Variational and projection methods for the
 527 volume constraint in finite deformation elasto-plasticity, Computer Meth-
 528 ods in Applied Mechanics and Engineering 51 (1985) 177–208.
- 529 [18] C. R. Dohrmann, P. B. Bochev, A stabilized finite element method for the
 530 Stokes problem based on polynomial pressure projections, International
 531 Journal for Numerical Methods in Fluids 46 (2004) 183–201.
- 532 [19] C. Lovadina, F. Auricchio, On the enhanced strain technique for elasticity
 533 problems, Computers & Structures 81 (2003) 777–787.
- 534 [20] K.-J. Bathe, The inf-sup condition and its evaluation for mixed finite ele-
 535 ment methods, Computers & Structures 79 (2001) 243–252.
- 536 [21] T. J. R. Hughes, Multiscale phenomena: Green's functions, the Dirichlet-
 537 to-Neumann formulation, subgrid scale models, bubbles and the origins of
 538 stabilized methods, Computer Methods in Applied Mechanics and Engi-
 539 neering 127 (1995) 387–401.

- 540 [22] A. Masud, K. Xia, A Stabilized MixedFinite Element Method for Nearly
 541 IncompressibleElasticity, *Journal of Applied Mechanics* 72 (2005) 711–720.
- 542 [23] R. Rossi, R. Zorrilla, R. Codina, A stabilised displacement-volumetric
 543 strain formulation for nearly incompressible and anisotropic materials,
 544 *Computer Methods in Applied Mechanics and Engineering* 377 (2021)
 545 113701.
- 546 [24] E. Karabelas, M. A. F. Gsell, G. Haase, G. Plank, C. M. Augustin, An
 547 accurate, robust, and efficient finite element framework with applications to
 548 anisotropic, nearly and fully incompressible elasticity, *Computer Methods in Applied
 549 Mechanics and Engineering* 394 (2022) 114887.
- 550 [25] T. J. R. Hughes, L. P. Franca, M. Balestra, A new finite element formulation
 551 for computational fluid dynamics: V. Circumventing the babuška-
 552 brezzi condition: A stable Petrov-Galerkin formulation of the stokes prob-
 553 lem accommodating equal-order interpolations, *Computer Methods in Applied
 554 Mechanics and Engineering* 59 (1986) 85–99.
- 555 [26] D. N. Arnold, F. Brezzi, M. Fortin, A stable finite element for the Stokes
 556 equations, *CALCOLO* 21 (1984) 337–344.
- 557 [27] F. Auricchio, L. Beirão da Veiga, C. Lovadina, A. Reali, A stability study of
 558 some mixed finite elements for large deformation elasticity problems, *Com-
 559 puter Methods in Applied Mechanics and Engineering* 194 (2005) 1075–
 560 1092.
- 561 [28] A. Quarteroni, A. Valli, *Numerical Approximation of Partial Differential Equations*, Springer Series in Computational Mathematics, Springer, Berlin, 1994.
- 562 [29] M. Crouzeix, P. Raviart, Conforming and nonconforming finite element
 563 methods for solving the stationary Stokes equations I, *Revue française
 564 d'automatique informatique recherche opérationnelle. Mathématique* 7
 565 (1973) 33–75.
- 566 [30] U. Brink, E. Stein, On some mixed finite element methods for incompress-
 567 ible and nearly incompressible finite elasticity, *Computational Mechanics*
 568 19 (1996) 105–119.
- 569 [31] T. Belytschko, Y. Y. Lu, L. Gu, Element-free Galerkin methods, *Internation-
 570 al Journal for Numerical Methods in Engineering* 37 (1994) 229–256.
- 571 [32] W. K. Liu, S. Jun, Y. F. Zhang, Reproducing kernel particle methods,
 572 *International Journal for Numerical Methods in Fluids* 20 (1995) 1081–
 573 1106.
- 574 [33] S. W. Chi, J. S. Chen, H. Y. Hu, A weighted collocation on the strong form
 575 with mixed radial basis approximations for incompressible linear elasticity,
 576 *Computational Mechanics* 53 (2014) 309–324.

- 579 [34] L. Wang, Z. Qian, Y. Zhou, Y. Peng, A weighted meshfree collocation
 580 method for incompressible flows using radial basis functions, *Journal of*
 581 *Computational Physics* 401 (2020) 108964.
- 582 [35] A. Ortiz-Bernardin, M. Puso, N. Sukumar, Improved robustness for nearly-
 583 incompressible large deformation meshfree simulations on Delaunay tes-
 584 sellations, *Computer Methods in Applied Mechanics and Engineering* 293
 585 (2015) 348–374.
- 586 [36] T. J. Hughes, J. A. Cottrell, Y. Bazilevs, Isogeometric analysis: CAD,
 587 finite elements, NURBS, exact geometry and mesh refinement, *Computer*
 588 *Methods in Applied Mechanics and Engineering* 194 (2005) 4135–4195.
- 589 [37] F. Auricchio, L. Beirão da Veiga, C. Lovadina, A. Reali, The importance
 590 of the exact satisfaction of the incompressibility constraint in nonlinear
 591 elasticity: Mixed FEMs versus NURBS-based approximations, *Computer*
 592 *Methods in Applied Mechanics and Engineering* 199 (2010) 314–323.
- 593 [38] A. Huerta, S. Fernández-Méndez, Locking in the incompressible limit for
 594 the element-free Galerkin method, *International Journal for Numerical*
 595 *Methods in Engineering* 51 (2001) 1361–1383.
- 596 [39] J. Dolbow, T. Belytschko, Volumetric locking in the element free Galerkin
 597 method, *International Journal for Numerical Methods in Engineering* 46
 598 (1999) 925–942.
- 599 [40] G. Moutsanidis, J. J. Koester, M. R. Tupek, J.-S. Chen, Y. Bazilevs, Treat-
 600 ment of near-incompressibility in meshfree and immersed-particle methods,
 601 *Computational Particle Mechanics* 7 (2020) 309–327.
- 602 [41] G. Moutsanidis, W. Li, Y. Bazilevs, Reduced quadrature for FEM, IGA
 603 and meshfree methods, *Computer Methods in Applied Mechanics and En-*
 604 *gineering* 373 (2021) 113521.
- 605 [42] Z.-Y. Wang, Y.-F. Jin, Z.-Y. Yin, Y.-Z. Wang, Overcoming volumetric
 606 locking in stable node-based smoothed particle finite element method with
 607 cubic bubble function and selective integration, *International Journal for*
 608 *Numerical Methods in Engineering* 123 (2022) 6148–6169.
- 609 [43] J. S. Chen, S. Yoon, H. P. Wang, W. K. Liu, An improved reproducing
 610 kernel particle method for nearly incompressible finite elasticity, *Computer*
 611 *Methods in Applied Mechanics and Engineering* 181 (2000) 117–145.
- 612 [44] C. M. Goh, P. M. F. Nielsen, M. P. Nash, A stabilised mixed mesh-
 613 free method for incompressible media: Application to linear elasticity and
 614 Stokes flow, *Computer Methods in Applied Mechanics and Engineering* 329
 615 (2018) 575–598.

- 616 [45] D. S. Bombarde, M. Agrawal, S. S. Gautam, A. Nandy, Hellinger–Reissner
617 principle based stress–displacement formulation for three-dimensional iso-
618 geometric analysis in linear elasticity, Computer Methods in Applied Me-
619 chanics and Engineering 394 (2022) 114920.
- 620 [46] A. Huerta, Y. Vidal, P. Villon, Pseudo-divergence-free element free
621 Galerkin method for incompressible fluid flow, Computer Methods in Ap-
622 plied Mechanics and Engineering 193 (2004) 1119–1136.
- 623 [47] C. Wu, W. Hu, J. Chen, A meshfree-enriched finite element method for
624 compressible and near-incompressible elasticity, International Journal for
625 Numerical Methods in Engineering 90 (2012) 882–914.
- 626 [48] E. Stein, R. de Borst, T. J. R. Hughes (Eds.), Encyclopedia of Compu-
627 tational Mechanics, John Wiley, Chichester, West Sussex, 2004.
- 628 [49] I. Babuška, J. Osborn, Eigenvalue Problems, in: Handbook of Numerical
629 Analysis, Vol. 2 of Finite Element Methods (Part 1), Elsevier, 1991, pp.
630 641–787.
- 631 [50] K. Yosida, Functional Analysis, 6th Edition, Classics in Mathematics,
632 Springer-Verlag, Berlin Heidelberg, 1995.
- 633 [51] S. Timoshenko, J. Goodier, Theory of Elasticity, Engineering Mechanics
634 Series, McGraw-Hill, 1969.